



Cite this: *Mater. Adv.*, 2025,
6, 9220

Received 29th August 2025,
Accepted 13th October 2025

DOI: 10.1039/d5ma00976f

rsc.li/materials-advances

Valley spin-splitting in pristine and Cr- and Ni-doped HfN_2 monolayers

Nguyen Thi Han ^a and Vo Khuong Dien *^b

Using first-principles calculations, we systematically studied the spin-orbit coupling (SOC)-induced valley spin splitting in a pristine HfN_2 monolayer ($\text{HfN}_2\text{-ML}$) and in Cr- and Ni-doped systems. The pristine $\text{HfN}_2\text{-ML}$ is revealed to host a direct band gap at the K and K' points of the Brillouin zone. The valley spin splitting reaches 350 meV for the conduction bands and 83.5 meV for the valence bands. Furthermore, the exciton binding energy of the $\text{HfN}_2\text{-ML}$ is estimated to be approximately 0.90 eV. The exciton ground states belong to the Wannier–Mott type, which are governed by the electron and hole band edge states. More importantly, the valley spin at the K and K' points could substantially change the effects when Cr or Ni is doped into the $\text{HfN}_2\text{-ML}$. Consequently, the Cr-doped HfN_2 monolayer exhibits a pronounced Zeeman splitting of approximately 300 meV. These findings highlight the promise of the $\text{HfN}_2\text{-ML}$ and related two-dimensional (2D) materials for prospective applications in valleytronic and spintronic devices.

1. Introduction

Nowadays, valleytronics focuses on exploiting and manipulating the valley degree of freedom in electronic materials, offering promising opportunities for future electronic, optoelectronic, and spintronic applications.^{1–4} Unlike conventional electronic materials, valleytronic materials offer advantages, such as high speed and low power consumption.¹ This is attributed to the presence of two or more local energy extremes in the occupied and unoccupied states, offering opportunities for encoding, storing, or processing diverse information.⁵ Recently, the transition metal dichalcogenides (TMDs), such as MoS_2 and WSe_2 monolayers, have garnered attention for their prominent valley properties^{6–8} and have been the subject of extensive study for valleytronic applications.

Beyond TMDs, other 2D materials have also emerged as promising candidates for valleytronic and spintronic applications, owing to their rich electronic structures, tunable interlayer couplings, and the possibility of engineering symmetry breaking through external fields or selective doping.⁹ Like TMDs, transition metal nitride semiconductors have garnered considerable interest^{10–12} owing to their exceptional properties.^{13–16} Moreover, extensive efforts have been devoted to doping in 2D systems as an effective strategy to tailor their electronic and magnetic

properties, thereby opening avenues for prospective applications in spintronics and valleytronics devices.¹⁷

Hafnium dinitride (HfN_2) represents one of the materials attracting substantial interest. Bulk HfN_2 has been reported to exhibit remarkable ductility, and thin films of HfN_x have been successfully fabricated using the through-silicon-*via* technology.¹⁸ Although experimental efforts toward the synthesis of 2D HfN_2 are still ongoing, the stability of the $\text{HfN}_2\text{-ML}$ has been established theoretically.¹⁹ It's generating significant interest due to its unique properties, such as optical, electronic, and structural characteristics.^{19–21} In particular, the $\text{HfN}_2\text{-ML}$ is emerging as a candidate for exploring new possibilities in valleytronics.^{22,23} Using first-principles calculations, substrate-induced excellent electronic properties in $\text{HfN}_2\text{-ML}$ have been observed in the literature, such as $\text{CrS}_2/\text{HfN}_2$ ²⁴ and $\text{MoTe}_2/\text{HfN}_2$.²⁵ However, there has been a scarcity of comprehensive investigations into $\text{HfN}_2\text{-ML}$ up to now, encompassing both theoretical calculations and experimental measurements related to the properties of valley electronics and excitonic properties. Additionally, the effects of doping transition metal elements on the $\text{HfN}_2\text{-ML}$ -induced enriched valley properties have not yet been explored.

In this work, we systematically investigate the intrinsic electronic and excitonic properties of pristine $\text{HfN}_2\text{-ML}$, along with the remarkable electronic modifications induced by chromium (Cr) and nickel (Ni) doping, using first-principles calculations. The $\text{HfN}_2\text{-ML}$ exhibits several key characteristics: (i) a moderate direct band gap of 4.20 eV at the K and K' valleys, accompanied by distinct conduction- and valence-band splittings; (ii) strong excitonic effects arising from its unique band dispersion and non-uniform dielectric screening; and (iii)

^a Department of Basic Science, Hung Yen University of Technology and Education, Hung Yen, Vietnam

^b FPT University, Can Tho campus, Can Tho city, Vietnam.
E-mail: vkdien@fpt.edu.vn



pronounced valley-spin polarization at the K and K' points upon Cr and Ni doping, leading to a significant Zeeman-type splitting. These results highlight HfN₂-ML as a promising 2D material for next-generation spintronic, valleytronic, and optoelectronic applications. Moreover, Cr dopants introduce net magnetic moments into the otherwise nonmagnetic HfN₂-ML, offering an effective route to realize spin-polarized functionalities for practical spintronic device applications.

2. Calculational methods

This work was performed on the investigated materials using first-principles calculations.^{26,27} The projector augmented-wave (PAW)

method was employed to represent the ionic potential.²⁸ For the description of exchange-correlation interactions, the generalized gradient approximation (GGA) in the form of Perdew–Burke–Ernzerhof (PBE) was used.^{29,30} The calculations utilized a plane wave cut-off energy of 500 eV,³¹ ensuring convergence with energy precision of 10^{-8} eV³² and a force precision of 2×10^{-3} eV Å⁻¹. A vacuum slab with a thickness of 20 Å was implemented to prevent spurious interactions along the z-direction. A sampling of the Brillouin zone was achieved using a Γ -centered k -mesh grid of $25 \times 25 \times 1$. The SOC^{33,34} was considered to calculate the electronic band structure and optical properties due to the heavy Hf element.³⁵ We have employed the single-shot G_0W_0 method applied to Kohn–Sham wave functions³⁶ to obtain quasi-electronic band structures utilizing a k -point grid of $15 \times 15 \times 1$ and a

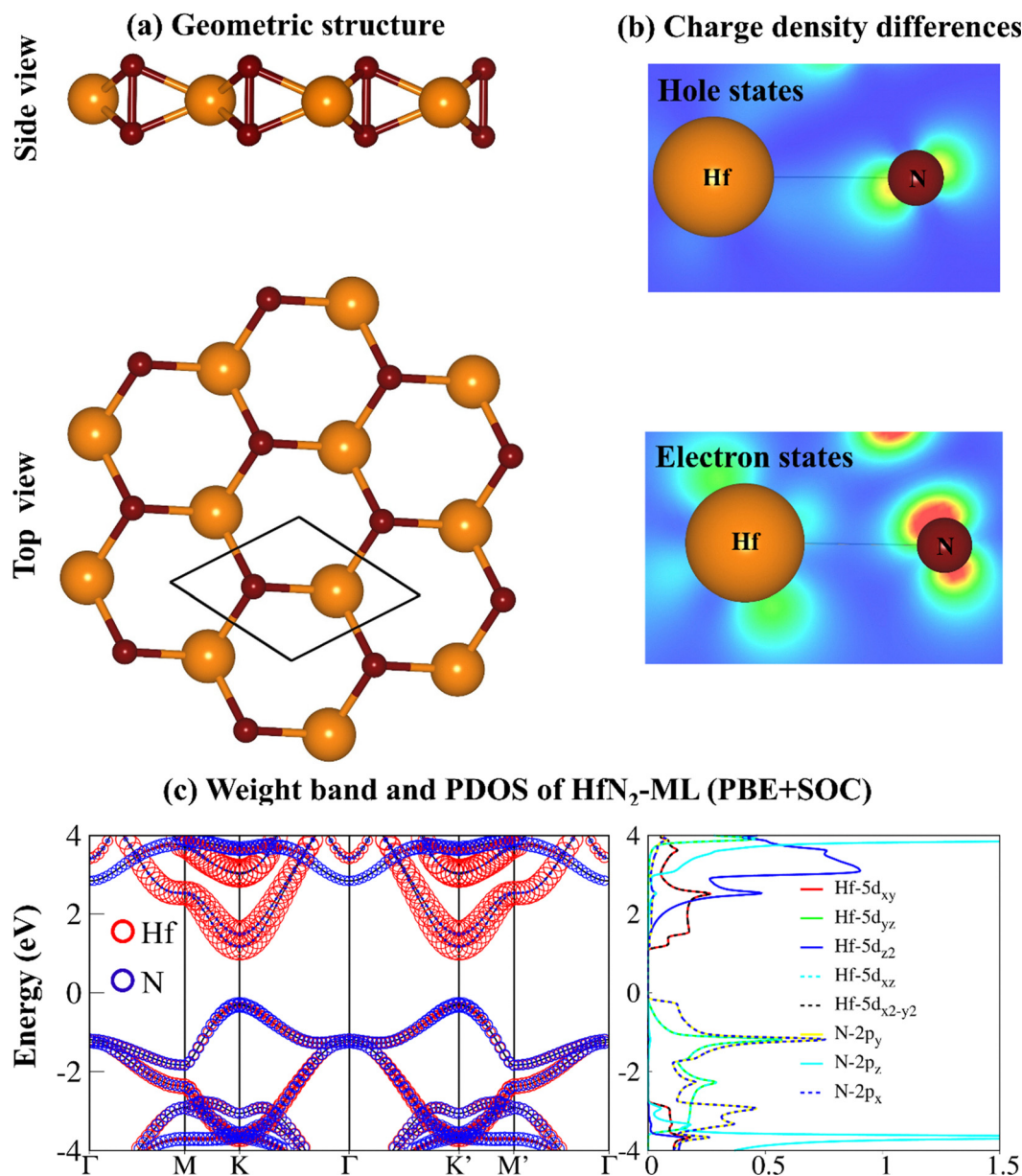


Fig. 1 (a) Optimized structure of 2D HfN₂-ML (side and top views), (b) band-decomposed charge densities at the valence-band maximum and conduction-band minimum, and (c) band weights and projected density of states (PDOS) obtained from PBE + SOC.

response function cutoff energy of 120 eV. To accurately determine the exciton spectrum, we systematically explored the convergence behavior of the Bethe–Salpeter equation (BSE),³⁷ focusing on parameters such as the number of k -points and the electron–hole pairs involved. Our findings suggest that achieving convergence involves utilizing a k -point grid of $25 \times 25 \times 1$ and accounting for the four highest occupied and the three lowest unoccupied states for pristine HfN_2 .

On the other hand, the Berry curvature^{38,39} is defined as $\Omega_n(k) = i \left\langle \frac{\partial}{\partial k} u_{n,k} \right| \times \left| \frac{\partial}{\partial k} u_{n,k} \right\rangle$, where $u_{n,k}$ and k represent the Bloch function and wave vector, respectively. For an applied in-plane electric field, this Berry curvature gives rise to an anomalous velocity $v_{\perp} = -\frac{e}{\hbar} E \times \Omega(k)$, which drives the charge carriers at the K and K' points in opposite directions. The Berry curvature is calculated from the wave functions *via* WANNIER90,⁴⁰

$$\Omega_n(k) = - \sum_{(n' \neq n)} \frac{2\text{Im} \langle \psi_{n,k} | v_x | \psi_{n',k} \rangle \langle \psi_{n',k} | v_y | \psi_{n,k} \rangle}{(E_{n'} - E_n)^2}$$

where $v_{x,y}$ are the velocity operators, and the summation is over all the occupied states. By applying an in-plane electric field and optical selection rule, charge, spin, and valley Hall current can be effectively manipulated, which has great potential for valleytronic applications.

3. Results and discussion

Fig. 1a presents the top and side views of the HfN_2 -ML. The optimized lattice parameters are $a = b = 3.38 \text{ \AA}$, in good agreement with previously reported values.^{20,21,23} According to prior publications,^{19,41} HfN_2 -ML exhibits excellent thermal, dynamical, and mechanical stability, as confirmed by *ab initio* molecular-dynamics simulations, phonon dispersion, and elastic-constant analyses. These results indicate that the HfN_2 -ML is structurally stable and suitable for further doping studies.

The electronic band structures, calculated at the GW level including spin–orbit coupling (SOC), reveal a direct band gap of 4.20 eV located at the K and K' points, as shown in Fig. 2a. The blue and red curves represent the spin-up and spin-down states, respectively. The band dispersion of the HfN_2 -ML

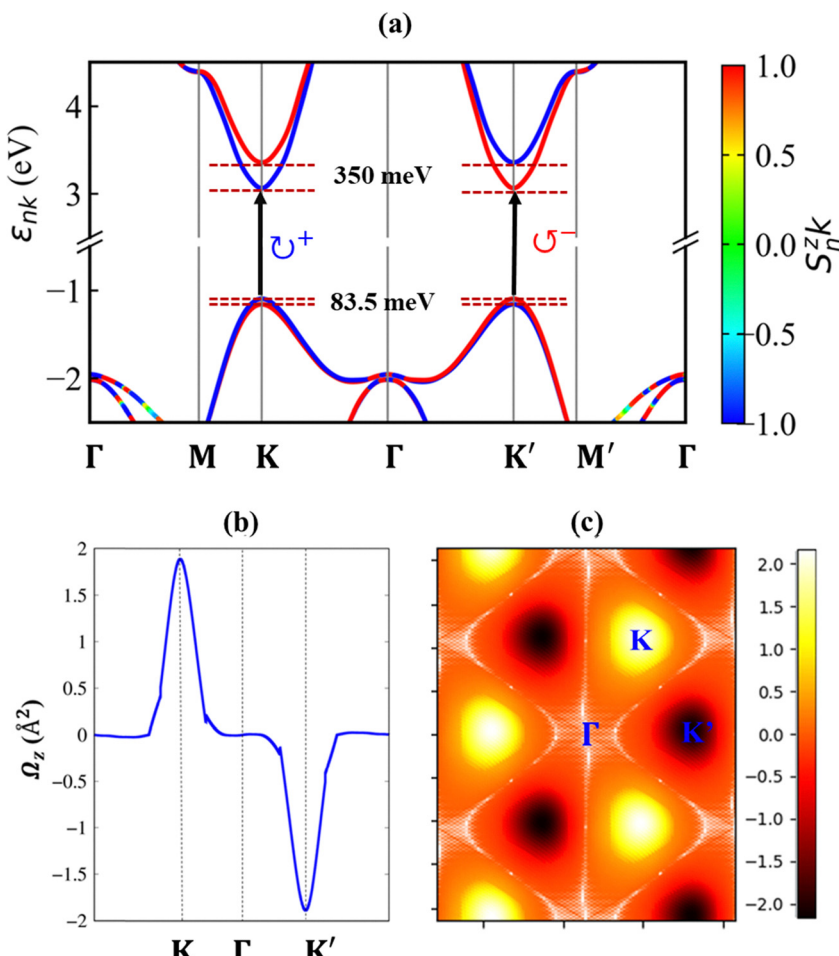


Fig. 2 (a) Energy band structure of HfN_2 -ML calculated at the GW level including spin–orbit coupling (SOC), showing the spin-resolved (spin-projected) bands. The black arrows indicate the optical transitions corresponding to left- and right-handed circularly polarized light (σ^+ and σ^-), (b) Berry curvature of HfN_2 -ML plotted along the high-symmetry path in the Brillouin zone, and (c) 2D distribution of Berry curvature in momentum space.



exhibits a pronounced valley spin splitting (VSS) of approximately 350 meV in the conduction band and a smaller VSS of about 83.5 meV in the valence band. Interestingly, this trend is opposite to that observed in conventional transition-metal dichalcogenides (TMDs), where the valence-band VSS dominates. For comparison, the VSS in monolayer MoS₂ and WSe₂ is about 150 meV and 430 meV, respectively, while the corresponding conduction-band splitting is nearly negligible.⁴² The distinct SOC-induced splittings in the valence and conduction bands originate from the different orbital characters of the underlying Bloch states. Specifically, the valence band is primarily derived from the N-(2p_x, 2p_y) orbitals, whereas the conduction band is dominated by the Hf-(5d_{xy}, 5d_{x²-y²}) orbitals. These orbital contributions are clearly reflected in the band-decomposed charge densities and the orbital-resolved projected density of states (PDOS), as shown in Fig. 1b and c.

The spin ordering at the K and K' valleys is opposite; consequently, carriers in these valleys can be selectively excited by circularly polarized light following opposite optical selection rules, as indicated by the black arrows in Fig. 2a. It is worth

noting that the spin-split states at the K and K' valleys remain energetically degenerate rather than significantly lifted. This subtle degeneracy stems from the underlying time-reversal symmetry that intrinsically connects the two valleys. Nevertheless, the absence of inversion symmetry in HfN₂-ML leads to opposite Berry curvatures for charge carriers at the K and K' points, as clearly shown in Fig. 2b and c. This valley-contrasting Berry curvature not only reveals the nontrivial topological nature of the electronic bands, but also offers a promising route for manipulating valley-dependent charge transport and optical selection in this system.

Fig. 3 shows the optical absorption spectra of HfN₂-ML obtained from GW and GW-BSE calculations including SOC. In Fig. 3a, the imaginary part of the dielectric function, $\epsilon_2(\omega)$, computed within the GW-RPA framework (black), is compared with that obtained from the GW-BSE approach (red), which explicitly incorporates electron-hole interactions. Two pronounced absorption peaks, labeled A and B and located near 5.8 and 6.0 eV, respectively, correspond to bright resonant excitons that dominate the optical response above the

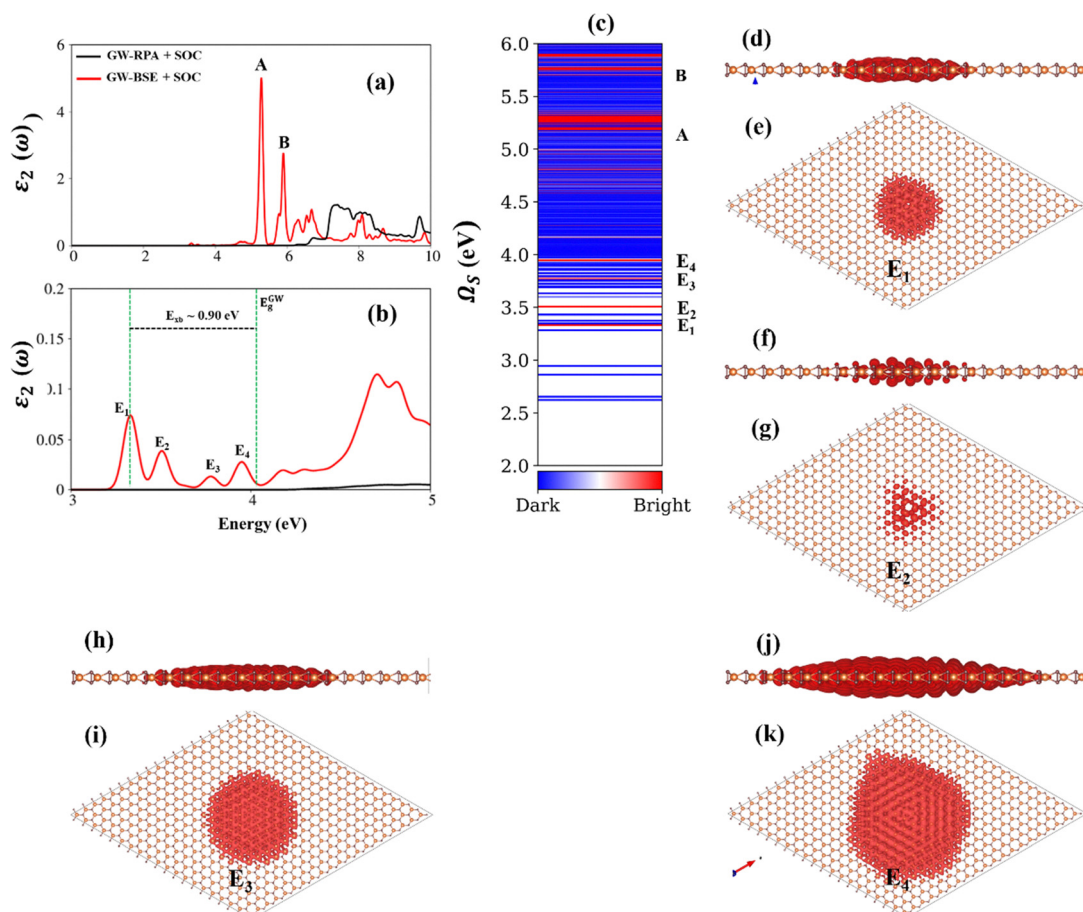


Fig. 3 (a) and (b) The imaginary part of the dielectric functions, depicting the impact of excitonic effects (GW-BSE, represented by the solid red line) and without excitonic effects (GW-RPA, shown by the solid black line), covering the energy range from 0.0 eV to 10.0 eV, including an enlarged view within the 3.0 eV to 5.0 eV energy range. (c) exciton energy levels of HfN₂-ML, derived by the GW-BSE method. Optically bright exciton states are highlighted in red, while dark exciton states are depicted in blue. (d)–(k) Representation of exciton amplitudes in real space, showcasing iso-value surfaces of the amplitude square, with the value set at 0.0003 of the maximum value. The upper panel provides a side view, while the lower panel offers a top view. Specific representations include (d)–(k) exciton E_1 – E_4 .

quasiparticle band gap. The inclusion of electron-hole interactions markedly enhances these features, highlighting the strong excitonic effects in this material. Fig. 3b focuses on the low-energy region, where four bound excitonic states (E_1 – E_4) are identified below the GW quasiparticle band gap with a large binding energy of approximately 0.90 eV, primarily arising from transitions at the K and K' valleys. This value exceeds those reported for typical transition-metal dichalcogenides (TMDs), such as MoS₂ (0.54 eV)⁴³ and WS₂ (0.71 eV),⁴⁴ indicating enhanced Coulomb interactions and reduced dielectric screening in HfN₂-ML. The excitons E_1 – E_4 exhibit relatively small but finite oscillator strengths, as shown in Fig. 3c, suggesting that they are weakly bright (quasi-dark) due to spin-orbit-induced mixing and the lack of inversion symmetry. Fig. 3d–k illustrates the real-space exciton wavefunctions of these four lowest bound states from both side and top views. The excitonic wavefunctions are spatially well confined within a few unit cells, confirming their Wannier-Mott character, consistent with the exciton localization observed in monolayer TMDs.^{45,46}

To investigate the influence of doping on the valleytronic properties of HfN₂-ML, we substitute transition-metal atoms into the pristine system. Specifically, Cr and Ni atoms are selected as dopants, with a single Cr or Ni atom replacing one Hf atom in a $4 \times 4 \times 1$ supercell of HfN₂-ML to model the doping effect. The choice of Cr and Ni is motivated by their partially filled 3d orbitals, which can introduce localized magnetic moments and significantly enhance SOC. These characteristics are crucial for valleytronics, as they enable the

breaking of time-reversal and inversion symmetries, leading to valley splitting and spin-valley polarization. Upon doping, the Cr-doped HfN₂-ML becomes spin-polarized, whereas the Ni-doped system remains non-spin polarized. The calculated total magnetic moments are $-1.937\mu_B$ for Cr-doped HfN₂-1L and $0.000\mu_B$ for Ni-doped HfN₂-ML, respectively. This contrasting behavior originates from their distinct electronic configurations: the Cr-3d orbitals lie near the Fermi level and strongly hybridize with Hf-d and N-p states, resulting in exchange splitting and stabilization of a ferromagnetic ground state. In contrast, the Ni-3d orbitals are positioned deeper in the valence region, exhibiting weak hybridization near the band edges, which suppresses spin polarization and leads to a nonmagnetic ground state.

The charge density difference ($\Delta\rho$) is plotted in Fig. 4a, and defined as $\Delta\rho = \rho_{\text{Cr}/\text{Ni}-\text{HfN}_2} - \rho_{\text{Cr}/\text{Ni}} - \rho_{\text{HfN}_2}$, where $\rho_{\text{Cr}/\text{Ni}-\text{HfN}_2}$, ρ_{HfN_2} , and $\rho_{\text{Cr}/\text{Ni}}$ represent the charge densities of the Cr- or Ni-doped HfN₂-ML, the pristine HfN₂-ML, and the isolated Cr or Ni atoms, respectively, in the same spatial configuration. The resulting maps reveal pronounced charge accumulation and depletion regions primarily localized at the doping interface, confirming strong orbital hybridization between the dopant and the host lattice. Bader charge analysis further shows that approximately 2.50 (2.40) electrons are transferred from Cr (Ni) to the HfN₂-ML, indicating significant charge redistribution and covalent bonding characteristics. To gain deeper insight into the magnetic behavior, the spin density distribution of the Cr-doped HfN₂-ML is presented in Fig. 4b. The spin density is

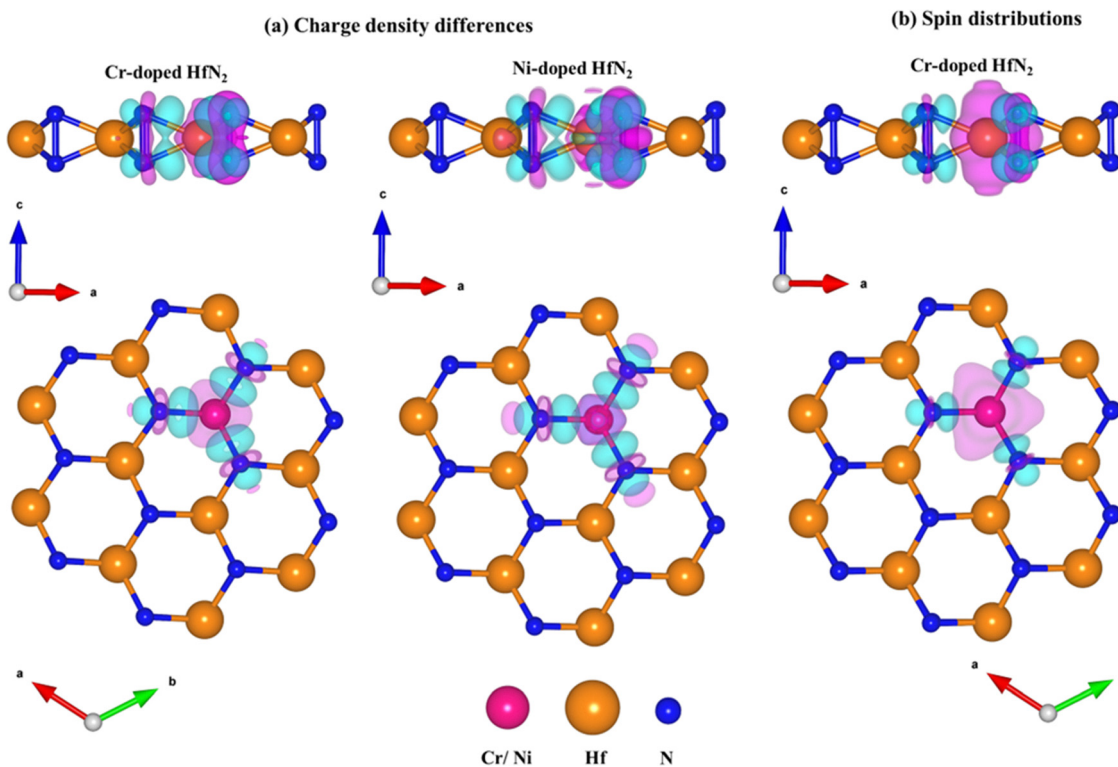


Fig. 4 (a) Side view and top view of the charge density differences of Cr-/Ni-doped HfN₂-1L, and (b) spin distributions of Cr-doped HfN₂, respectively. Note: the pink and cyan iso-surfaces are 0.002.



mainly concentrated around the Cr dopant site, while contributions from the surrounding Hf and N atoms are relatively minor, confirming that the magnetic moment predominantly originates from the localized Cr-3d states.

Fig. 5a presents the density of states (DOS) of the pristine HfN_2 -ML, calculated at the PBE level without SOC. For comparison, Fig. 5b and c display the DOS of the Cr- and Ni-doped HfN_2 -ML, respectively, obtained using the same theoretical level of theory. Upon Cr doping (Fig. 5b), a ferromagnetic ground state emerges, as indicated by the distinct spin-resolved orbital contributions of Cr, Hf, and N atoms in both

the valence and conduction regions. This behavior aligns with the spin-density distributions in Fig. 4b, where a clear asymmetry between spin-up and spin-down channels is evident. The induced magnetism originates from spin-dependent splitting of the valence states and the localization of Cr-3d orbitals near the Fermi level (E_F), which enhances exchange interactions and mediates spin polarization among neighboring Hf and N atoms. Such orbital hybridization and energy-level rearrangement reveal that Cr doping not only stabilizes long-range ferromagnetic order but also substantially modifies the electronic structure near E_F , thereby offering a mechanism to tailor

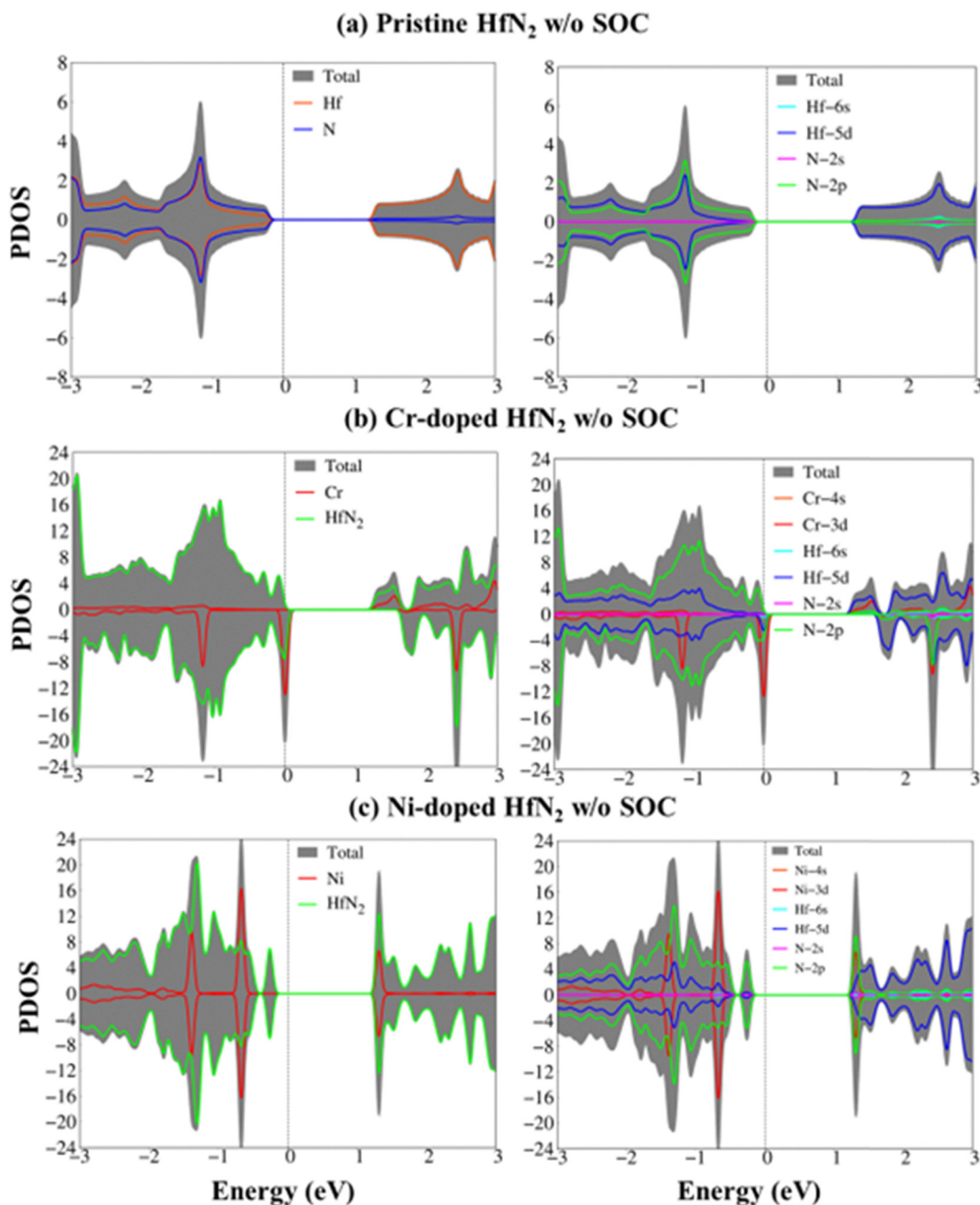


Fig. 5 (a) The van Hove singularities in the density of states (DOS) without (w/o) SOC of pristine HfN_2 , corresponding to (b) and (c) doping Cr, and Ni atoms in HfN_2 -ML, respectively.



the spintronic functionality of HfN_2 -ML. Specifically, the adsorption of Cr introduces an n-type character, as Cr-3d orbitals donate additional electrons close to the conduction-band edge, shifting the Fermi level upward and producing a metallic response in the spin-polarized DOS. Ni-doped HfN_2 -ML in Fig. 5c, on the other hand, retains nonmagnetic and semiconducting characteristics. The nearly symmetric van Hove singularities in the spin-up and spin-down DOS closely mirror those of the pristine HfN_2 -ML, confirming the absence of exchange splitting and net magnetic moment. The electronic structure thus remains dominated by the host Hf-d and N-p states. Consequently, while Cr incorporation enables the formation of spin-polarized states and magnetic ordering, Ni doping primarily alters the band dispersion, serving instead as an effective route to tune the electronic transport properties without breaking time-reversal symmetry.

Fig. 6a–c present the PBE + SOC band structures of the pristine, Cr-doped, and Ni-doped HfN_2 -ML. The corresponding magnified views focusing on the valence band dispersions near the Fermi level are shown in Fig. 6d–f. As illustrated in Fig. 6a, the pristine HfN_2 -ML exhibits distinct band-edge features

around the K and K' valley points. The calculated parameters, including the valley Zeeman splitting (E_z), valley splitting (Δ_v), and spin splitting ($\Delta_{\text{spin},v}$) at the K and K' valleys for the pristine, Cr-doped, and Ni-doped HfN_2 -ML are summarized in Table 1. The valley Zeeman splitting is given by $E_z = \Delta_{\text{opt}}^+ - \Delta_{\text{opt}}^-$, where Δ_{opt}^+ and Δ_{opt}^- correspond to the optical transition energies under left- and right-circularly polarized light (σ^+ and σ^-), respectively. Notably, in the Cr-doped HfN_2 -ML, the emergence of magnetic ordering breaks time-reversal symmetry and lifts the valley degeneracy, resulting in a pronounced Zeeman splitting of $E_z = 300$ meV. In contrast, the Ni-doped system, being nonmagnetic, preserves the valley degeneracy, consistent with its absence of spin polarization.

4. Conclusions

In summary, based on first-principles calculations, we have investigated the valley properties and excitonic states of monolayer HfN_2 , as well as the effects of Cr and Ni doping on its electronic structure. The pristine HfN_2 -ML exhibits a direct

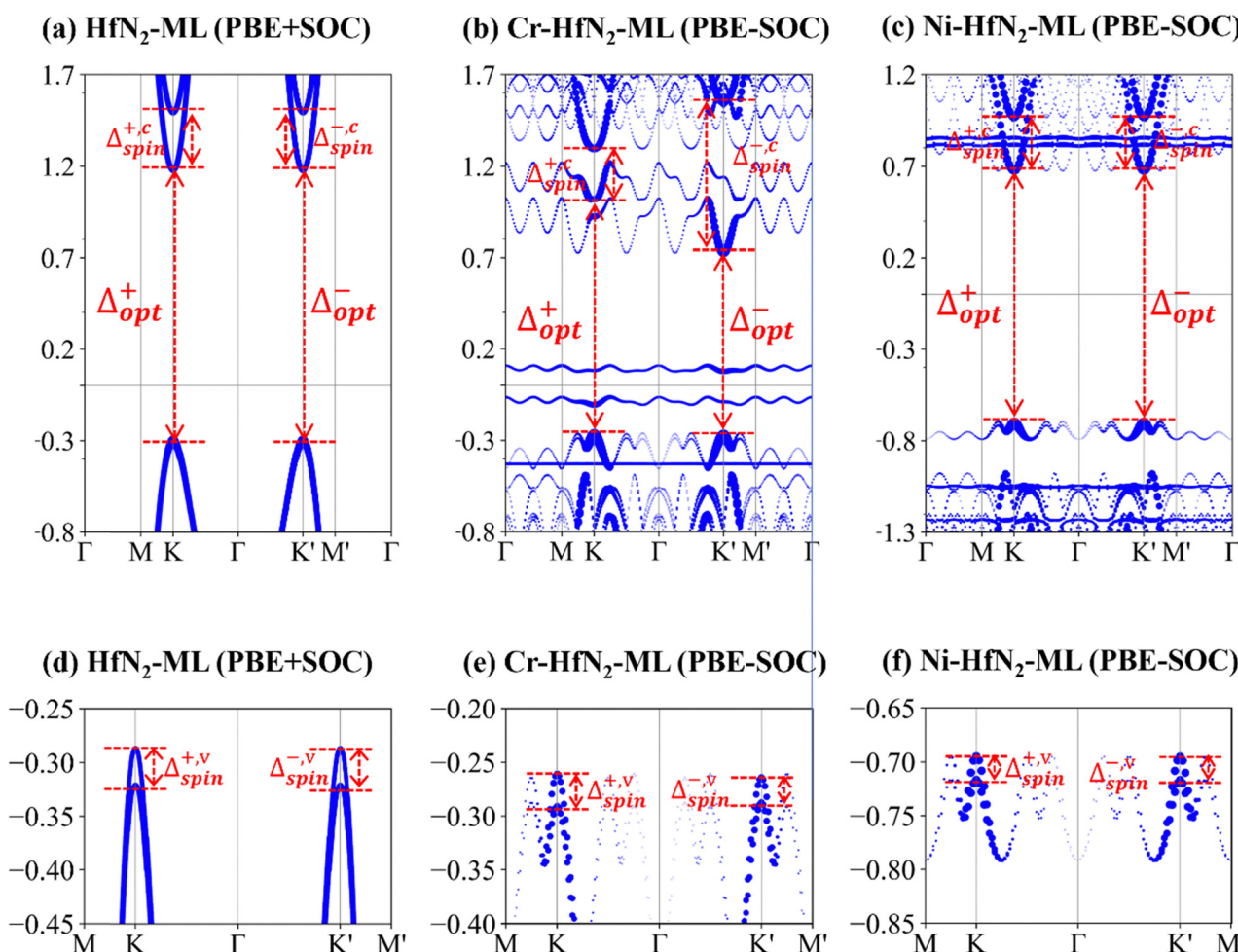


Fig. 6 (a) Energy band structure of the pristine HfN_2 -ML obtained with PBE + SOC; (b) and (c) unfolded electronic band structures of the Cr- and Ni-doped HfN_2 -ML, respectively, obtained using the vaspkit code.⁴⁷ Panels (d)–(f) show the corresponding enlarged band structures in the valence bands.

Table 1 Calculated optical and spin–valley parameters of HfN_2 -ML under Cr and Ni doping, obtained under the DFT + SOC level of theory. Listed are the energies of the σ^+ (σ^-) circularly polarized absorption edges corresponding to the excitonic transitions Δ_{opt}^+ (Δ_{opt}^-), the spin splittings of the conduction and valence bands ($\Delta_{\text{spin},c}^\pm$ and $\Delta_{\text{spin},v}^\pm$), and the valley Zeeman splitting (E_z). The symbols “+” and “–” represent quantities at the K and K' valleys, respectively, while “c” and “v” denote the conduction and valence bands. All energies are expressed in meV

System	$\Delta_{\text{spin}}^{+,v}$	$\Delta_{\text{spin}}^{-,v}$	$\Delta_{\text{spin}}^{+,c}$	$\Delta_{\text{spin}}^{-,c}$	Δ_{opt}^+	Δ_{opt}^-	E_z
Pristine HfN_2	40.0	40.0	400	400	1450	1450	0
Cr-doped HfN_2	35.0	30.0	300	800	1150	850	300
Ni-doped HfN_2	25.0	25.0	350	350	1350	1350	0

band gap located at the K and K' valleys. Remarkably, pronounced VSSs of 350 meV and 83.5 meV are obtained in the conduction and valence bands, respectively, primarily originating from strong SOC. Two bright resonant excitons (A and B) appear near 5.8 and 6.0 eV, while four bound excitonic states (E_1 – E_4) are identified below the quasiparticle gap with a large binding energy of approximately 0.90 eV, indicating strong Coulomb interactions and reduced dielectric screening. Furthermore, Cr and Ni doping significantly modify the valley–spin characteristics at the K and K' valleys through SOC-induced interactions. These results deepen the theoretical understanding of valleytronic and excitonic phenomena in 2D materials and underscore the potential of doped HfN_2 -MLs for next-generation electronic, spintronic, and valleytronic applications.

Conflicts of interest

The authors declare no competing interests.

Data availability

All data supporting the findings of this study are available within the article. This includes numerical data underlying all figures and tables, structural models, and representative input files used in the calculations. Additional details regarding computational parameters and analysis procedures are fully described in the Computational details section.

References

- 1 S. A. Vitale, *et al.*, Valleytronics: opportunities, challenges, and paths forward, *Small*, 2018, **14**(38), 1801483.
- 2 J. R. Schaibley, *et al.*, Valleytronics in 2D materials, *Nat. Rev. Mater.*, 2016, **1**(11), 1–15.
- 3 K. F. Mak, D. Xiao and J. Shan, Light–valley interactions in 2D semiconductors, *Nat. Photonics*, 2018, **12**(8), 451–460.
- 4 A. Molina-Sánchez, D. Sangalli, L. Wirtz and A. Marini, Ab initio calculations of ultrashort carrier dynamics in two-dimensional materials: valley depolarization in single-layer WSe₂, *Nano Lett.*, 2017, **17**(8), 4549–4555.
- 5 H.-K. Li, *et al.*, Valley optomechanics in a monolayer semiconductor, *Nat. Photonics*, 2019, **13**(6), 397–401.

- 6 Z. Wang, J. Shan and K. F. Mak, Valley-and spin-polarized Landau levels in monolayer WSe₂, *Nat. Nanotechnol.*, 2017, **12**(2), 144–149.
- 7 G. Wang, *et al.*, Valley dynamics probed through charged and neutral exciton emission in monolayer WSe₂, *Phys. Rev. B: Condens. Matter Mater. Phys.*, 2014, **90**(7), 075413.
- 8 G. Kioseoglou, A. Hanbicki, M. Currie, A. Friedman, D. Gunlycke and B. Jonker, Valley polarization and inter-valley scattering in monolayer MoS₂, *Appl. Phys. Lett.*, 2012, **101**(22), 221907.
- 9 Y. Qi, J. Zhao and H. Zeng, Tunable spin/valley splitting and multiple Hall effects in interlayer coupling-dependent SVSiN₂ multiferroic bilayers, *Appl. Phys. Lett.*, 2025, **126**(11), 112106.
- 10 S. Anand, K. Thekkedath and U. V. Waghmare, Two-dimensional rectangular and honeycomb lattices of Nbn: emergence of piezoelectric and photocatalytic properties at nanoscale, *Nano Lett.*, 2016, **16**(1), 126–131.
- 11 Z. Liu, J. Liu and J. Zhao, YN₂ monolayer: Novel p-state Dirac half metal for high-speed spintronics, *Nano Res.*, 2017, **10**, 1972–1979.
- 12 J. Li, G. Gao, Y. Min and K. Yao, Half-metallic YN₂ monolayer: dual spin filtering, dual spin diode and spin Seebeck effects, *Phys. Chem. Chem. Phys.*, 2016, **18**(40), 28018–28023.
- 13 S. Gong, C. Zhang, S. Wang and Q. Wang, Ground-state structure of YN₂ monolayer identified by global search, *J. Phys. Chem. C*, 2017, **121**(18), 10258–10264.
- 14 C. Zhang, J. Liu, H. Shen, X.-Z. Li and Q. Sun, Identifying the ground state geometry of a MoN₂ sheet through a global structure search and its tunable p-electron half-metallicity, *Chem. Mater.*, 2017, **29**(20), 8588–8593.
- 15 Y. Wei, Y. Ma, W. Wei, M. Li, B. Huang and Y. Dai, Promising photocatalysts for water splitting in ben₂ and mgn₂ monolayers, *J. Phys. Chem. C*, 2018, **122**(15), 8102–8108.
- 16 B. Wang, Q. Wu, Y. Zhang, L. Ma and J. Wang, Auxetic B4N monolayer: a promising 2D material with in-plane negative Poisson's ratio and large anisotropic mechanics, *ACS Appl. Mater. Interfaces*, 2019, **11**(36), 33231–33237.
- 17 J. Zhao, Y. Qi, C. Yao and H. Zeng, Tunable valley–spin splitting in a Janus XM SiN₂ monolayer (X= S, Se; M= Mo, Cr) and giant valley polarization via vanadium doping, *Phys. Rev. B*, 2024, **109**(3), 035408.
- 18 M. B. Takeyama, M. Sato, E. Aoyagi and A. Noya, Preparation of nanocrystalline HfNx films as a thin barrier for through-Si via interconnects in three-dimensional integration, *Jpn. J. Appl. Phys.*, 2014, **53**(2S), 02BC05.
- 19 Y. Sun, B. Xu and L. Yi, HfN₂ monolayer: A new direct-gap semiconductor with high and anisotropic carrier mobility, *Chin. Phys. B*, 2020, **29**(2), 023102.
- 20 A. Betal, M. Alam, J. Bera, H. Meghnani, A. N. Gandi and S. Sahu, Excellent optoelectronic and thermoelectric properties of two-dimensional transition metal dinitride HfN₂, *Phys. B*, 2023, **649**, 414505.
- 21 M. K. Mohanta, I. Fathima and A. De Sarkar, Exceptional mechano-electronic properties in the HfN₂ monolayer: a



promising candidate in low-power flexible electronics, memory devices and photocatalysis, *Phys. Chem. Chem. Phys.*, 2020, **22**(37), 21275–21287.

22 M. K. Mohanta and A. De Sarkar, Coupled spin and valley polarization in monolayer Hf N 2 and valley-contrasting physics at the Hf N 2–WS e 2 interface, *Phys. Rev. B*, 2020, **102**(12), 125414.

23 B. Zhai, *et al.*, Using ferroelectric polarization to regulate and preserve the valley polarization in a HfN 2/CrI 3/In 2 Se 3 heterotrilayer, *Phys. Rev. B*, 2021, **103**(21), 214114.

24 M. K. Mohanta, H. Seksaria and A. J. A. S. S. De Sarkar, Insights into CrS2 monolayer and n-CrS2/p-HfN2 interface for low-power digital and analog nanoelectronics, *Appl. Surf. Sci.*, 2022, **579**, 152211.

25 M. K. Mohanta, A. Rawat and A. J. A. S. S. De Sarkar, Atomistic manipulation of interfacial properties in HfN2/MoTe2 van der Waals heterostructure via strain and electric field for next generation multifunctional nanodevice and energy conversion, *Appl. Surf. Sci.*, 2021, **568**, 150928.

26 J. Hafner, Ab-initio simulations of materials using VASP: Density-functional theory and beyond, *J. Comput. Chem.*, 2008, **29**(13), 2044–2078.

27 G. Kresse and J. Furthmüller, Computational Materials 10, *Science*, 1996, **6**, 15–50.

28 P. E. Blochl, Projector augmented-wave method, *Phys. Rev. B: Condens. Matter Mater. Phys.*, 1994, **50**(24), 17953–17979.

29 J. P. Perdew, K. Burke and M. Ernzerhof, Perdew, burke, and ernzerhof reply, *Phys. Rev. Lett.*, 1998, **80**(4), 891.

30 J. P. Perdew, K. Burke and M. Ernzerhof, Generalized gradient approximation made simple, *Phys. Rev. Lett.*, 1996, **77**(18), 3865.

31 M. Otani and O. Sugino, First-principles calculations of charged surfaces and interfaces: A plane-wave nonrepeated slab approach, *Phys. Rev. B: Condens. Matter Mater. Phys.*, 2006, **73**(11), 115407.

32 G. Te Velde and E. Baerends, Precise density-functional method for periodic structures, *Phys. Rev. B: Condens. Matter Mater. Phys.*, 1991, **44**(15), 7888.

33 A. Manchon and S. J. P. R. B. Zhang, Theory of spin torque due to spin-orbit coupling, *Phys. Rev.*, 2009, **79**(9), 094422.

34 R. J. J. P. R. Elliott, Theory of the effect of spin-orbit coupling on magnetic resonance in some semiconductors, *Phys. Rev. B*, 1954, **96**(2), 266.

35 B. T. Zhou, K. Taguchi, Y. Kawaguchi, Y. Tanaka and K. T. Law, Spin-orbit coupling induced valley Hall effects in transition-metal dichalcogenides, *Commun. Phys.*, 2019, **2**(1), 26.

36 I. G. Ryabinkin, S. V. Kohut and V. N. Staroverov, Reduction of electronic wave functions to Kohn-Sham effective potentials, *Phys. Rev. Lett.*, 2015, **115**(8), 083001.

37 D. Y. Qiu, F. H. da Jornada and S. G. Louie, Solving the Bethe-Salpeter equation on a subspace: Approximations and consequences for low-dimensional materials, *Phys. Rev. B*, 2021, **103**(4), 045117.

38 M. Gradhand, D. Fedorov, F. Pientka, P. Zahn, I. Mertig and B. Györffy, First-principle calculations of the Berry curvature of Bloch states for charge and spin transport of electrons, *J. Phys.: Condens. Matter*, 2012, **24**(21), 213202.

39 J. Son, K.-H. Kim, Y. Ahn, H.-W. Lee and J. Lee, Strain engineering of the Berry curvature dipole and valley magnetization in monolayer MoS₂, *Phys. Rev. Lett.*, 2019, **123**(3), 036806.

40 G. Pizzi, *et al.*, Wannier90 as a community code: new features and applications, *J. Phys.: Condens. Matter*, 2020, **32**(16), 165902.

41 M. Dimple, A. R. Mohanta, N. Rawat, R. Jena, A. Ahammed and A. De Sarkar, Ultra-low lattice thermal conductivity and giant phonon-electric field coupling in hafnium dichalcogenide monolayers, *J. Phys.: Condens. Matter*, 2020, **32**, 315301.

42 D. Xiao, G.-B. Liu, W. Feng, X. Xu and W. Yao, Coupled spin and valley physics in monolayers of MoS₂ and other group-VI dichalcogenides, *Phys. Rev. Lett.*, 2012, **108**(19), 196802.

43 K. Wang and B. J. P. C. C. P. Paulus, Tuning the binding energy of excitons in the MoS₂ monolayer by molecular functionalization and defective engineering, *Phys. Chem. Chem. Phys.*, 2020, **22**(21), 11936–11942.

44 B. Zhu, X. Chen and X. Cui, Exciton binding energy of monolayer WS₂, *Sci. Rep.*, 2015, **5**(1), 9218.

45 M. H. Naik, *et al.*, Intralayer charge-transfer moiré excitons in van der Waals superlattices, *Nature*, 2022, **609**(7925), 52–57.

46 I. B. Amara, E. B. Salem and S. J. S. Jaziri, Optoelectronic response and interlayer exciton features of MoS₂/WS₂ van der Waals heterostructure within first principle calculations and Wannier Mott model, *Superlattices Microstruct.*, 2017, **109**, 897–904.

47 V. Wang, N. Xu, J.-C. Liu, G. Tang and W.-T. Geng, VASPKIT: A user-friendly interface facilitating high-throughput computing and analysis using VASP code, *Comput. Phys. Commun.*, 2021, **267**, 108033.

